Heavy-duty UAV Electrical Propulsion Architectures and Multi-timescale Multi-physics Modeling

Yue Cao[1] and Alastair P. Thurlbeck[2]
Oregon State University, Corvallis, OR 97331, USA

This paper demonstrates the application of static, dynamic, and thermal modeling to all-electric vertical take-off and landing unmanned aerial vehicles (VTOL UAVs). The paper emphasizes on the electrical propulsion systems of the heavy-duty commercial multi-copter aircraft. The multi-timescale modeling approach allows for analysis of propulsion power losses, efficiencies, and flight-times as well as the dynamic behaviors of the electro-mechanical system. Since the maximum temperature of the motor windings is a critical design limit, thermal modeling is used to estimate stator winding temperature based on power losses and propeller speeds. The static, dynamic, and thermal models can be combined with a realistic flight mission profile to study craft performance under various flight stages effectively.

I. Introduction

As vertical take-off and landing unmanned aerial vehicles (VTOL UAVs) become utilized in broader commercial applications, the power levels and payload capacity of the UAV result in new challenges [1]. Conventionally, UAVs used by enthusiasts or in cinematography applications are small in size and have little additional mass beyond the mass of the craft itself. However, when a sizeable payload is added, such as in a package delivery [2]-[4] or passenger transporting [5] application, a significant increase in thrust and craft power levels is required. Flight-time is reduced due to the increased power demand. The energy storage mass and its energy capacity may also be limited. Thus there is a trade-off between flight-time and payload capacity, the optimum allocation of which is application specific. Optimizing the power system design for maximum efficiency is therefore essential for heavy duty UAVs. Accurate power system modeling also allows optimum component selection based on required voltage and current ratings. If components are underspecified, overheating issues or device failure may cause poor reliability or catastrophic craft failure. On the other hand, if components are over specified, the craft design will have wasted mass, and thus a reduced flight-time or payload. In such commercial applications, the reliability and redundancy of the UAV are also critical. Thus the thermal performance, fault tolerance, and control of the craft must be given careful consideration.

As shown in [6], static modeling of the UAV power system can estimate component and system power losses and efficiency. The model of the power system also allows for sizing of energy storage based on desired flight-time as well as other power system parameter optimizations. This paper builds on this static modeling framework [6] by adding dynamic simulation and thermal modeling elements, creating a comprehensive multi-timescale power system model. The dynamic simulation considers the response and stability of the DC-AC inverter and PMSM motor to rapid changes in motor speed and torque. Thermal modeling studies the temperature of the PMSM motor windings over time. In a non-propulsion application, the motor temperature would vary with the phase current according to the thermal capacitance of the windings. On the other hand, in a UAV application, the PMSM motor is designed such that the air pushed back by the propeller cools the motor windings. As the motor speed increases, the load torque increases and thus the phase current. At the same time, the air flow across the windings is also increased, cooling the windings more effectively. However, such a linked system behaves highly nonlinearly. Thermal modeling thus allows for this effect to be analyzed, and the temperature of the windings can be considered over a realistic mission profile.

---

[1] Assistant Professor, School of Electrical Engineering and Computer Science
[2] Graduate Student, School of Electrical Engineering and Computer Science

II. UAV Power System Overview

A generic UAV power system architecture consists of the following elements: power sources, DC-DC converters, a DC bus (DC link), DC-AC inverters, and propulsion motors. For this paper, auxiliary loads such as microcontrollers, control ICs, and the communication system are negligible, since their power consumption is insignificant compared to that of the propulsion motors.

In architecture 1 of Fig. 1, a DC-DC converter at the output of the battery allows for a fixed DC bus voltage. A fixed bus voltage allows the motors to be driven at their most efficient operating point and reduces I^2R losses in the DC bus. However, the DC-DC converter itself imposes extra power losses, weight, size, and cost. In architecture 2 of Fig. 1, the DC-DC converter is omitted, and the battery supplies the DC-AC inverters with a voltage that varies with battery state of charge (SOC) and load current, i.e., the DC bus voltage is the battery terminal voltage. Architecture 3 shows a hybrid battery/fuel cell system. A small battery responds to fast load dynamics and peak power demands while a fuel cell stack acts as the primary energy source, providing the majority of power during cruising and recharging the battery. The effects of architecture selection on system efficiency and flight-time are explained in detail in [6]. Thus this paper will consider only architecture 2 for conciseness. The transient response and thermal considerations are most critical at the PMSM motor and DC-AC
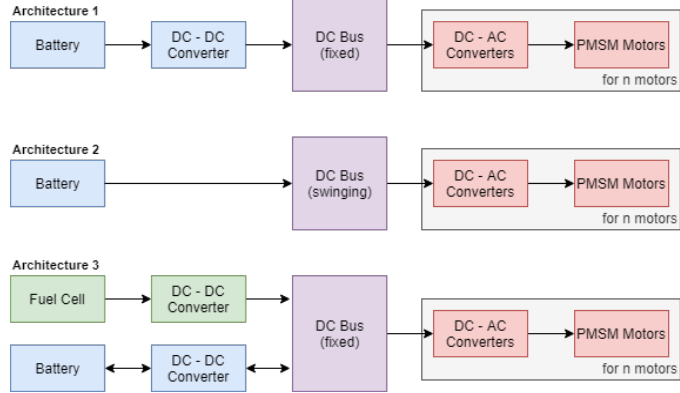

Fig. 1 Example UAV power system architectures. Architectures 1 and 2 use a battery as the primary energy source. In architecture 1 the battery voltage is boosted to a fixed DC bus voltage, whereas in architecture 2 the DC bus voltage is the varying battery voltage. Architecture 3 is a hybrid design in which a fuel cell stack is the primary energy source with a small battery as auxiliary storage.

inverter. Hence this paper will consider only the PMSM motor and DC-AC inverter during dynamic simulations and thermal modeling.

Brushless DC (BLDC) motors are often chosen to power small VTOL UAV's. However, as the aircraft size increases, permanent magnet surface mount (PMSM) motors offer reduced torque ripple and higher power density [7]. PMSM motors also offer a higher efficiency compared to other AC motors [8]. The PMSM motors modeled are out-runner style, surface-mounted permanent magnet (SPM) machines, though they are referred to more generally as PMSM in the remainder of this paper. Critically, the out-runner design allows for efficient rotor winding cooling due to the airflow pushed over the motor from the propeller. This effect is considered in the thermal modeling section of this paper.

The remaining elements of the UAV power system are the DC-DC and DC-AC converters. DC-DC converters are optional and allow conversion from the battery or fuel cell voltage to a fixed DC bus voltage as in architectures 1 and 3. A DC-AC inverter is required to drive the PMSM motors with three-phase AC from the DC bus. Various control and modulation schemes such as sinusoidal pulse width modulation (SPWM), 3rd harmonic injection, or space vector modulation (SVM) may be used in the inverter. In this paper, field-orientated control (FOC) and space vector modulation (SVM) are assumed.
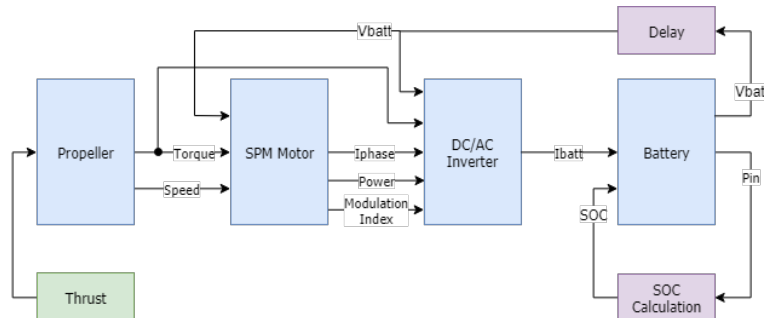

Fig. 2 Static modeling cascaded structure applied to architecture 2.

III. Static Modeling

1. Introduction

The static modeling of the UAV power system is detailed comprehensively in the authors' previous work [6]. Hence only the key equations governing each subsystem are presented in this paper. The general approach is to create a subsystem block containing the electrical equations of each block. Typically, the equations are used to calculate the total power loss in the subsystem, before calculating the required inputs for the following block based on known system parameters. Fig 2. Shows the static model structure and subsystem block connections.

2. PMSM Motors (Surface Mounted)

Fig. 3 shows the single-phase equivalent circuit model used for the surface mount PMSM motors. Stator resistance, R_s, and synchronous inductance, L_s, were measured experimentally. Phasor analysis in the d-q reference frame was used based on the method of [8], where the rotor magnet defines the reference, d-axis. The back EMF, $E_{ph(q)}$ is calculated as

$$E_{ph(q)} = k_e \cdot \omega_r$$

where ω_r is the rotor speed and k_e (Vs/rad) is the back EMF constant, calculated from the manufacturers specified motor constant, K_v (rpm/V). Electromechanical torque is given by

Fig. 3 Per phase equivalent circuit for a permanent magnet synchronous motor.

$$T_{em} = T_r + T_{nl}$$

where T_{nl} is the combined mechanical and core losses. T_r is the rotor or load torque applied to the motor from the propeller. With no field weakening, $I_{ph(d)} = 0$ and thus the phase current magnitude is calculated as

$$\left|I_{ph}\right| = I_{ph(q)} = \frac{T_{em}}{3 \cdot k_e}.$$

The d and q axis components and the magnitude of the phase voltage are given by

$$V_{ph(d)} = -\omega_r \cdot polepairs \cdot L_s \cdot I_{ph(q)}$$

$$V_{ph(q)} = E_{ph(q)} + R_s \cdot I_{ph(q)}$$

$$\left|V_{ph}\right| = \sqrt{V_{ph(d)}^2 + V_{ph(q)}^2}$$

where $polepairs$ is the number of magnetic pole pairs in the motor and thus relates rotor to electrical frequency. The modulation index, m_a is given by

$$m_a = \frac{2\sqrt{2} \cdot |V_{ph}|}{V_{bus}}.$$

3. DC-AC Inverters

It is assumed the DC-AC inverter is a hex bridge topology using field-orientated control (FOC) and space vector-modulation (SVM). The average switching current experienced by each MOSFET is the average of a half sinusoid:

$$I_{sw} = \frac{2\sqrt{2} \cdot I_{ph}'}{\pi}.$$

Where I_{ph}' is the phase current seen by a single MOSFET when there are $nump$ MOSFETs in parallel.

Switching voltage rise and fall times are calculated using the method of [9]. The current rise and fall times, tri and tfi, are given by the MOSFET manufacturer's datasheet. Switching losses in the MOSFET (q) and diode (d) are then calculated based on their respective turn on and turn off energies:

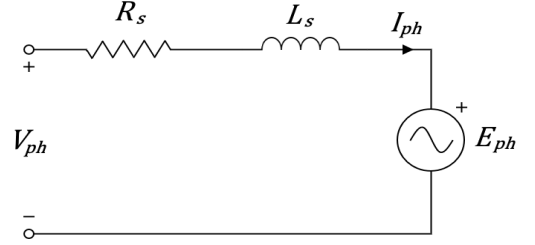$$E_{on(q)} = V_{bus} \cdot I_{sw} \cdot \frac{tri + tfv}{2} + Q_{rr} \cdot V_{bus}$$

$$E_{off(q)} = V_{bus} \cdot I_{sw} \cdot \frac{trv+tfi}{2}$$

$$E_{on(d)} = \frac{1}{4} \cdot Q_{rr} \cdot V_{bus}$$

where Q_{rr} is the body diode reverse recovery charge.

Average and RMS MOSFET and body diode currents are calculated according to [9, Appendix I], assuming Null = V0 switching. Then the MOSFET and body diode conduction losses are given by:

$$P_{on(q)} = I_{q(rms)}^2 \cdot R_{DSon}$$

$$P_{on(d)} = I_{d(ave)} \cdot V_f + I_{d(rms)}^2 \cdot R_{diode}$$

where R_{DSon} is the on resistance of the MOSFET, V_f the forward voltage drop of the body diode, and R_{diode} the on state resistance.

Switching losses are given by:

$$P_{sw(q)} = \left(E_{on(q)} + E_{off(q)}\right) \cdot \frac{f_{sw}}{2}$$

$$P_{sw(d)} = E_{off(d)} \cdot \frac{f_{sw}}{2}$$

where f_{sw} is the switching frequency of the inverter.

4. Lithium-Ion Battery Pack

The battery can be modeled dynamically using a three-time constant Randles' equivalent circuit [10] as shown in Fig. 4. Logarithmic-polynomial interpolation equations with coefficients from [10, Table II] are used to calculate the equivalent circuit elements as a function of battery state of charge (SOC):

$$\ln(V, R, C) = \sum_{k=0}^{6} a_k \cdot \ln^k(SOC)$$

For static simulation, capacitive elements are ignored and the resistances can then be summed together into an equivalent resistance, R_{static}. Since the cell tested in [10] had a specified maximum discharge rate of 1C, the resistance was decreased by a factor of 5 in order to support the required discharge rates of 5C or higher. The accuracy of the model should be increased by applying this equivalent circuit approach to an application specific high discharge rate Li-Po battery pack.
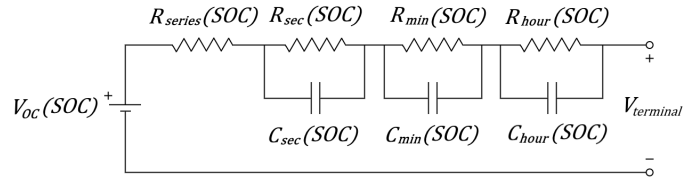

Fig. 4 Dynamic battery model from [10]. V, R and C elements are all functions of state of charge (SOC). For static simulation, capacitive elements are ignored and the resistive elements summed together.

IV. Dynamic Modeling

The d-q modeling of the PMSM machine is used to perform the dynamic simulation. The model is based on the d-q analysis presented in [11]. The d-axis is aligned with the rotor magnetic axis, and the q-axis current i_{sq} directly controls the motor torque. The d-axis current, i_{sd} is driven to zero. In other electric vehicle applications, a negative d-axis current may be used to work against the inherent magnetic flux from the motor permanent magnets. This field weakening effect allows higher speed operation; however, it is generally not required or desirable in a UAV application. The stator d-q winding voltages are given by:

$$v_{sd} = R_s \cdot i_{sd} + \frac{d}{dt}\lambda_{sd} - \omega_m \cdot \lambda_{sq}$$

$$v_{sq} = R_s \cdot i_{sq} + \frac{d}{dt}\lambda_{sq} + \omega_m \cdot \lambda_{sd}$$
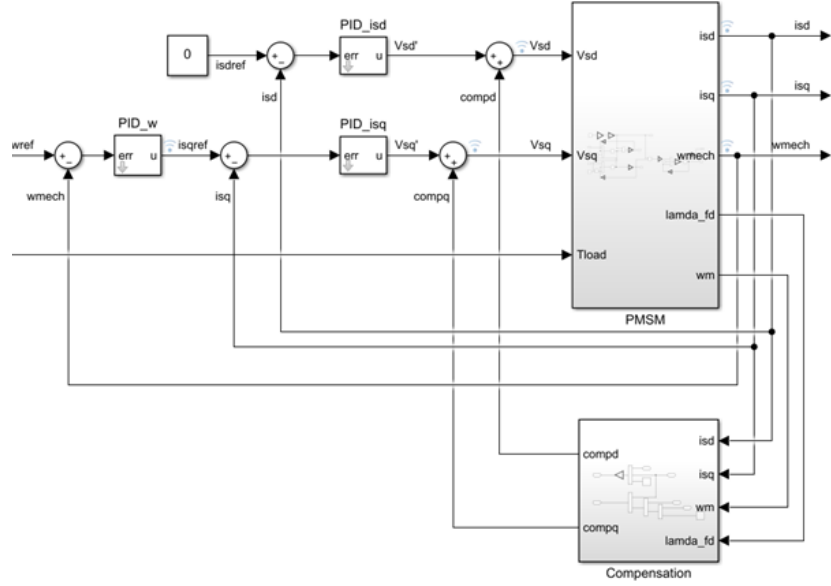
Fig. 5 Simulink for PMSM in the d-q reference frame. PI control loops are used to control motor speed and the d and q axis currents. The compensation terms compd and compq are used to decouple the current loops.

where R_s is the stator resistance, ω_m is the electrical speed of the motor and the d-q winding speed, $\omega_d = \omega_m$. Also λ_{sq} and λ_{sd} are the d and q winding flux linkages which are defined as

$$\lambda_{sd} = L_s \cdot i_{sd} + \lambda_{fd}$$

$$\lambda_{sq} = L_s \cdot i_{sq}$$

where λ_{fd} is the flux linkage due to the permanent magnets on the rotor. λ_{fd} is thus a constant and given by the motor constant. The electromagnetic torque generated is controlled by the q-axis current:

$$T_{em} = \frac{p}{2} \cdot \lambda_{fd} \cdot i_{sq}$$

where p is the number of magnetic poles. The acceleration of the motor is due to the net torque acting on the motor and propeller inertia, J:

$$J \cdot \frac{d\omega}{dt} = T_{em} - T_{load} - T_{friction}$$
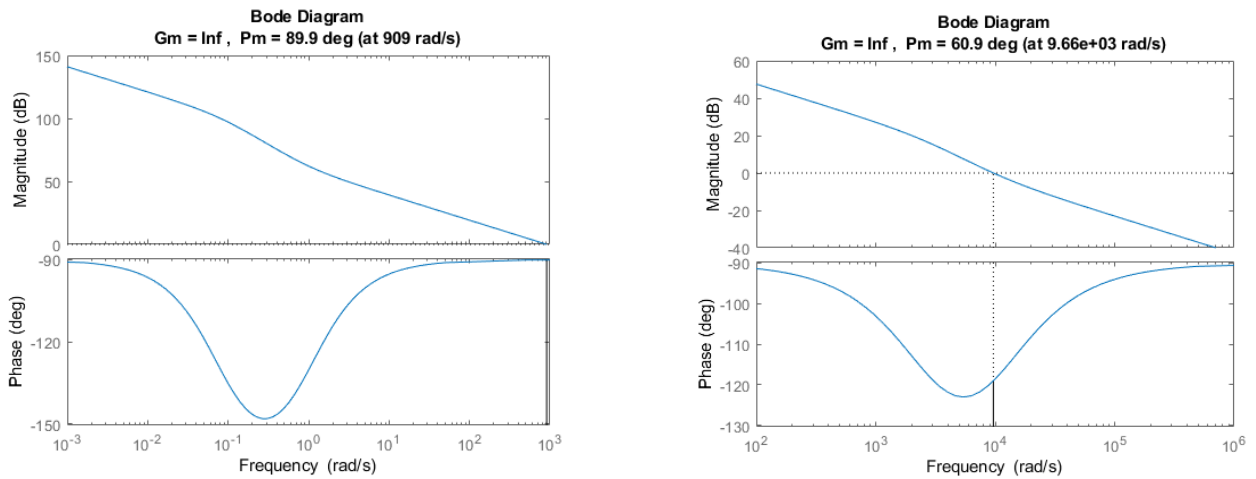

Fig. 6 Bode plots of the speed control loop (left) and d and q axis current control loops (right). The crossover frequency of the speed loop is at 95.2 Hz and the crossover frequency of both current loops at 1.01 kHz. The speed loop has a phase margin of 89.9°.

5

The above electrical and mechanical equations are used to create a Simulink model of the PMSM motor. Cascaded PI controllers for speed and current are then used to control the motor as shown in Fig. 5. The controller gains are selected to give the inner current loops a bandwidth of 1 kHz and the outer speed loop a bandwidth of 100 Hz. The bode plots of the speed and current loops are shown in Fig. 6.

The dynamic model is limited to the d-q reference frame, such that the high-frequency switching dynamics and modulation scheme of the DC-AC inverter are not modeled. However, the d-q model is effective in modeling the transient behavior of the motor considering the control loop behavior and stability as well as the electrical and mechanical properties of the motor.

V. Thermal Modeling

1. Basic Theoretical Approach

Thermal modeling is challenging as many theories apply to specific cooling conditions or object geometries. Often some thermal parameters must be obtained experimentally, adding lengthy processes and costs. The thermal model is important not only because it predicts maximum temperature for mechanical designs, but also because the temperature affects electrical parameters (e.g., winding resistance) in a significant way so that this, in turn, affects the electrical system behavior. A comprehensive system model must couple the two physical domains so that feedback and feedforward communications occur seamlessly. This section follows classical approaches of predicting air-cooled cylinders, since the motor assembles this geometry, and the spinning propeller provides the cooling air. Similar modeling work was published in another authors' paper [12] for more electric aircraft motor cooling systems.

Motor winding temperature is calculated based on the stator power losses passed from the above electrical model. A differential equation models the temperature change:

$$mc_p \frac{dT}{dt} = P_{loss} + h_a A_a (T_{amb} - T)$$

or the solution becomes

$$T = \frac{P_{loss} - c_0 e^{-\frac{A_a h_a t}{mc_p}} + A_a h_a T_{amb}}{A_a h_a} \tag{*}$$

where c_o is the initial condition in the form of

$$c_o = P_{loss} + [T_{amb} - T(0)] h_a A_a$$

and A_a is the heat transfer area of the motor winding, and h_a is the heat transfer coefficient, m is the heated mass, and c_p is the specific heat for thermal capacitance.

2. Steady-state Temperature Prediction

If only steady state info is needed, for example, as a feedback to the static model described in Section III, the exponential term is reduced to zero as time reaches infinity:

$$T = T_{ambient} + \frac{P_{loss}}{A_a * h_a}$$

In a numerical simulation, temperature calculation is an iterative process because its initial value must be assumed to run the first power loss calculation. Subsequent iterations reduce the assumed temperature error until reaching a numerically steady value.

It is challenging to find out the true A_a and h_a values. The area is calculated as the sum of the motor cylinder wall area and the ring area of the motor top and bottom:

$$A_a = \pi * D * L + 1/4 * \pi * (D^2 - D_{in}^2) * 2$$

where D is the outer diameter, D_{in} is the inner diameter, and L is the length (or height).

The heat transfer coefficient is calculated based on:

$$h = Nu \frac{k}{L}$$

where Nu is the Nusselt number for air, and k is the thermal conductivity for air, 0.0257 W/(mK). The Nusselt number is calculated using the Churchill-Bernstein relation because this relation applies to this particular geometry and cooling condition:

$$Nu = 0.3 + \frac{0.62 Re^{0.5} Pr^{0.333}}{[1 + (0.4/Pr)^{0.667}]^{0.25}} [1 + (Re/282000)^{0.625}]^{0.8}$$

where Re is the Reynolds number for air, Pr is the Prandtl number for air (0.707). The Reynolds number is calculated as

$$Re = \frac{\rho * v_{air} * D}{\mu_{air}}$$

where ρ is the air density, v_{air} is the effective air speed for cooling, which yet remains a challenge to determine, and μ_{air} is the absolute viscosity of air, 1.983×10^{-5} Ns/m². Note that other relations may be also suitable, but the general idea here is experimental-based assumption-heavy thermal equations are necessary.

3. *Transient Temperature Prediction*

The next step is to establish a model for transient dynamics that determine all the remaining values in eq. (*) at the beginning of this section. The challenge here is to experimentally tune the power loss and air speed values. An artificial "heating fraction coefficient" is introduced. The purpose of this coefficient is to correct the actual power going to heat the copper winding versus all the power losses calculated from the previous models. Another artificial "air fraction coefficient" follows. The purpose of this coefficient is to determine the equivalent air speed through the motor windings versus the full wind speed induced by the propeller. This allows us to link the calculated induced wind speed as part of the calculation. Once the heating fraction coefficient is determined, the value will be used for the air fraction coefficient's calculation. The two coefficients (ζ) are described in high level as

$$P_{loss} = P_{losstotal} \zeta_{heat}$$
$$v_{air} = v_{airtotal} \zeta_{air}$$

Both coefficients are determined through a hybrid experimental fitting and algorithm looping approach. The procedure is summarized as the following.

1) Heating fraction coefficient:

(i) Fit the collected temperature transient experiment data onto an exponential format. The curve fitting outputs an exponential coefficient in the form of "-k".

(ii) Select one experimental motor run with the following inputs: RPM, torque, time, initial temperature, final temperature, ambient temperature, and the above coefficient k.

(iii) With these input values, the coupled static model first calculates the motor power loss, which is multiplied by the heating fraction coefficient for the actual power that goes into the winding.

(iv) Iteration starts with an initial guess of the heating fraction coefficient. If this value is too large, the modeled final temperature will be higher than the actual final temperature, and the coefficient shall be reduced, and vice versa. Under each iteration, a final temperature is calculated from the starting temperature, total time, power loss, according to Forward Euler's integration method:

$$T(t + \Delta t) = T(t) + \Delta T(t)$$
$$\Delta T(t) = \frac{P_{loss} + H[T_{amb} - T(t)]}{mc_p} \Delta t$$

where $H = A_a h_a$.

(v) The loop iterates until it finds a heating fraction coefficient that produces modeled final temperature within 1 °C from the experimental final temperature.

(vi) Repeat the above steps for different experimental runs and then find an average value of the coefficient.

2) Air fraction coefficient:

(i)   A direct air speed value at the center of the motor must be given, which is either known through trustworthy measurement or calculated according to

$$v_{air} = v_i[1 + (\frac{z_1}{\sqrt{1 + z_1^2}})^p]$$

where

$$v_i = -0.5v_c + \sqrt{v_c^2 + \frac{T}{2\rho A}}$$

$$z_1 = z/R$$

where v_c is vehicle air speed (e.g., 0 for hover), z is the distance from the propeller plane (up-wash direction is negative), R is the propeller radius, T is the thrust in Newton, ρ is the air density (1.16 kg/m³), A is the circle area of the propeller, p is a coefficient of 0.6. These values and equations are obtained from [13].

(ii)   From an initial guess similar to the heating fraction coefficient process, the iteration will output a corrected air fraction coefficient so that the final temperature difference is within 1 °C. Inside the loop, the heat transfer coefficient (h) is calculated based on the guessed air fraction coefficient. This (h) later serves to calculate the final temperature based on motor mechanical and electrical losses.

(iii)   While calculating the electrical power loss, an additional loop is required because motor winding R_s changes each time with the temperature so that this loop matches the correct R_s and final temperature.

(iv)   Once both loops are complete, the corrected air fraction is the final output. Again repeat the above steps for different experimental runs and then find an average value of the coefficient.

VI. Simulation and Experimental Validation

A. Model Parameters

An example four-propeller VTOL UAV was designed to provide a sample application for the static and dynamic modeling. The system components and mass are outlined in Table I. The UAV was designed for a maximum continuous thrust of 24 kgf, which corresponds to 1.6 times the maximum loaded craft mass of 15 kg. The calculated unload mass is 11.24 kg, allowing a payload of 3.76 kg. The power system uses architecture 2 as shown in Fig. 1. The craft is designed to use T-motor U10II KV100 motors with G28x9.2 propellers and T-motor FOC ESCs (inverters). Since these components were experimentally tested, the relationship between craft thrust and motor speed and torque is realistic. The mass of the propellers, motors, and DC-AC inverters was specified by the manufacturer. Battery mass was calculated based on 3.7 V, 2200 mAh Lithium Polymer (Li-Po) cells in a 12-series 9-parallel configuration. The mass was then calculated from the capacity divided by the specific energy for a representative UAV Li-Po battery pack.

Wiring losses are calculated based on the mass per unit length of AWG10, AWG12, and AWG14 wires. For simplicity, wiring losses are calculated within the battery and DC-AC inverter models. Wiring loss is calculated as the I^2R loss based on the output current, wire size, wire quantity, and wiring length following the subsystem. Wiring losses are accounted for in the input power required by each subsystem but are not included in each subsystem's power loss and efficiency calculation. Instead, wiring losses are summed together to form a combined figure for system wiring loss.

Table I. VTOL UAV Component Mass Determination

Component	Data Source for Mass Calculation	Quantity	Mass (kg)
Propellers	T-Motor G28x9.2, specified mass.	4	0.392
Motors	T-Motor U10II KV100, specified mass.	4	1.660
Inverters (ESCs)	T-Motor Alpha 80A HV, specified mass.	4	0.440
Battery Pack	Tattu 10000mAh 6s 25C Li-Po, specific energy, Wh/kg,	-	5.543
Frame + Wiring	Estimation, approx. 20% of 15kg designed mass.	-	3.000
Aux Electronics	Estimation	-	0.200
Unloaded Craft Total (kg)			11.24
Payload			3.76
Loaded Craft Total (kg)			15

B. Experimental Validation of Models

The static model was compared to an experimental test of a T-motor Inverter (ESC), PMSM motor and propeller as detailed in [6]. The experimental testing was also used to determine the mechanical losses of the motor. This was then implemented in the static modeling of the motor, allowing the no load torque to be determined from a curve fitting of the experimental data. The experimental data also provided a mapping of motor speed to thrust and torque, enabling realistic mission profile simulations. Fig. 7 shows the experimental hardware setup.

The combined power losses of the DC-AC inverter (ESC) and PMSM motor were obtained using the static model and then compared to the actual combined power losses of the hardware as shown in Fig. 8. The static modeling showed considerable variation from the experimental values. However, it was determined to be sufficiently accurate for use in UAV power system design.
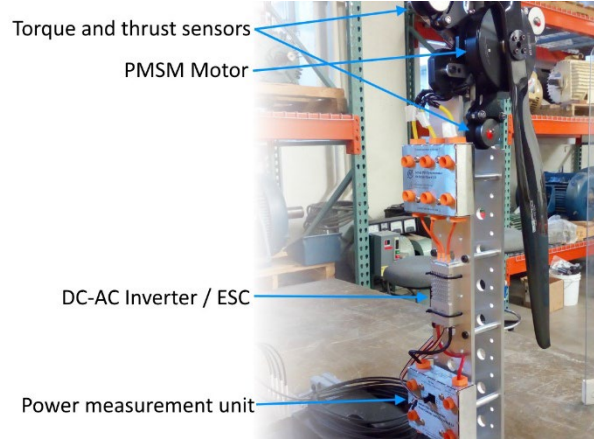

Fig. 7 Experimental setup consisting of a surface mount PMSM driven by a DC-AC inverter or electronic speed controller (ESC). A propeller applies a realistic load torque to the motor.
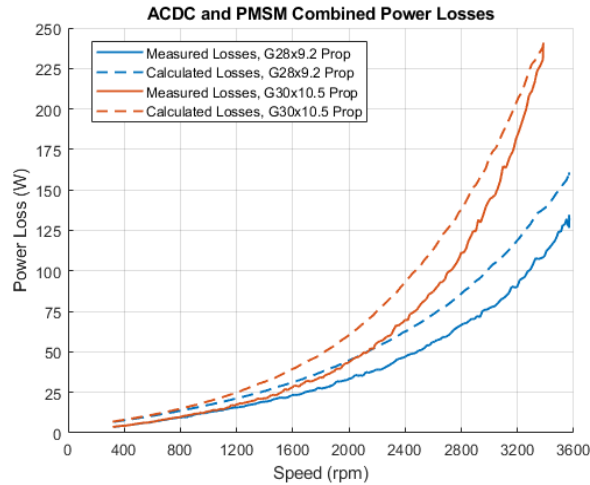

Fig. 8 Model calculated losses compared to the experimentally measured losses. The experiment was carried out with two propeller sizes. With the G28x9.2 propeller, the motor was swept to its rated speed whilst with the G30x10.5 propeller, the motor was swept to its rated current.

C. Mission Profile Based Simulations

The mission profile of Fig. 9 was applied to the static model of the sample VTOL UAV craft. This allows the simulation of the power system losses and efficiency over a realistic flight. In Fig. 9, normalized thrust is defined as the ratio of actual thrust to craft mass.

Fig. 10 shows the breakdown of power system losses by subsystem throughout the mission profile. The combined power system efficiency is also plotted. System efficiency is relatively constant throughout the flight, regardless of the flight stage. There is a slight reduction in efficiency during periods of reduced or increased thrust such as during ascending or descending. The system is most efficient during cruising. This is desirable, since the craft is cruising for the majority of the example flight. As expected the majority of the losses occur in the PMSM motor. Primarily this is due to resistive losses in the stator winding, which increase as the square of the phase current. Power losses in the battery pack are also relatively large. Similarly to the PMSM motor, the losses are mainly due to the internal cell resistance. Conversely, losses in the DC-AC inverter are more constant over the mission profile.
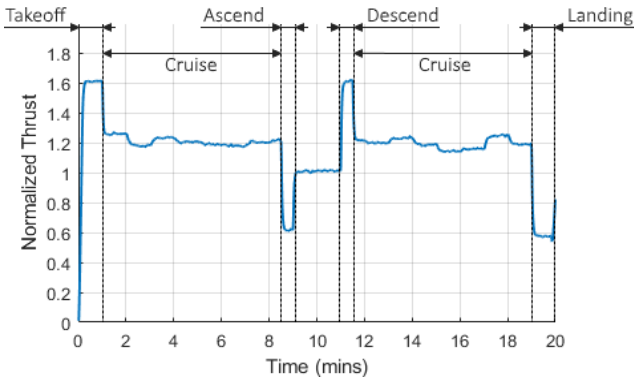
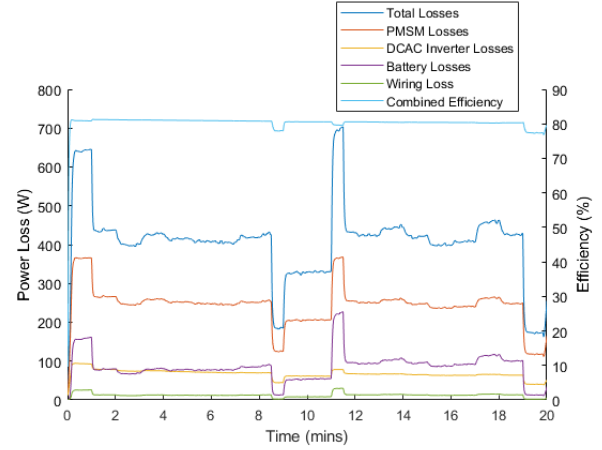**Fig. 7 Mission Profile including various flight stages.**

Fig. 10 Breakdown of power system losses and combined efficiency over the mission profile.

D. Dynamic Response

The dynamic model can be used to predict the response of the craft under disturbances or rapid changes in commanded motor speed. The motor parameters of the T-motor U10II PMSM motor determined in Section IV were applied to the dynamic model of Fig. 5. Often it is desirable for a controller to be simulated prior to hardware implementation. Thus the behavior of the control scheme presented in Section IV is investigated here as an example application of the model.

Typically in the VTOL UAV application, the microcontroller sends a speed command rather than a command for torque or thrust. Thus Fig. 11 shows the PMSM motor response to step changes in commanded speed. At $t = 2$ s, a step from zero to the rated speed (3600 RPM) is applied, and at $t = 7$ s, a step change back to zero is applied. The controller accurately tracks the commanded speed during both steps. The response time

Fig. 11 PMSM motor response to a commanded speed step from 0 to 3600 rpm.

is limited by the inertia of the motor and propeller and the maximum electromagnetic torque that can be generated in the motor. As the motor's mechanical speed increases, the propeller and thus load torque increases. The relationship between propeller speed and torque was obtained experimentally. The curve shape is not due to the controller response; instead, it is due to the reduced net torque and thus acceleration of the motor. The response to the negative step is much faster since torque acting on the motor remains positive, whereas now the electromagnetic torque is negative. The relationship between generated electromagnetic torque, load torque, and the net torque, $T_{net} = J \frac{d\omega}{dx}$ is shown in Fig. 12. Further, the d and q axis stator currents are plotted in Fig. 13.
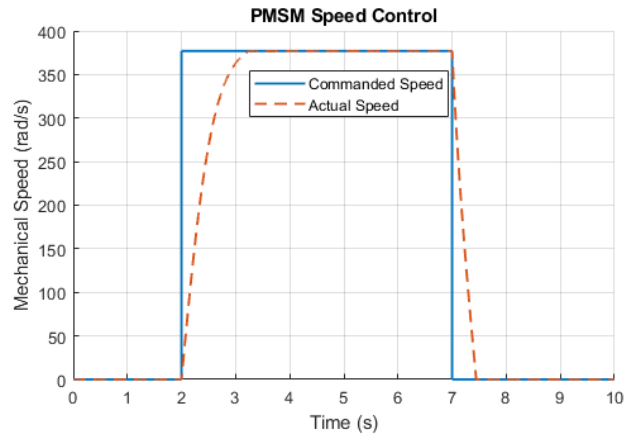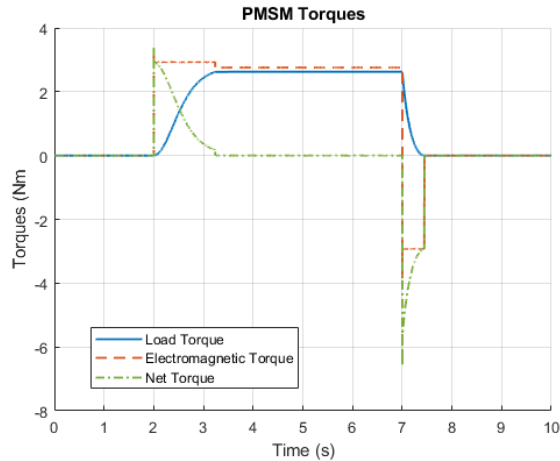
10

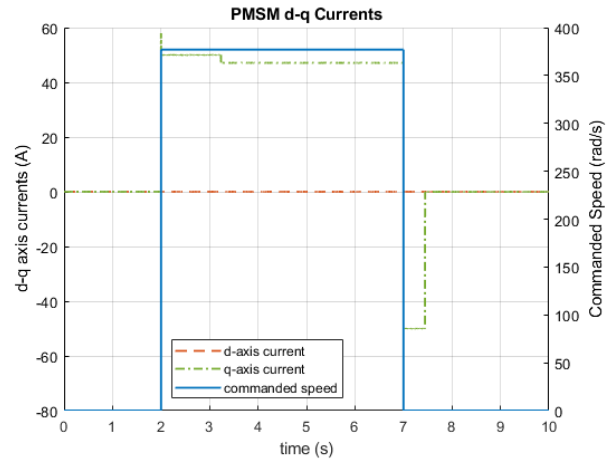**Fig. 12 Torques on the PMSM motor during the applied speed steps of Fig 11.**

Fig. 13 d and q axis stator currents in the PMSM motor during the applied speed steps.

E. Optimization Studies

Previous work [6] demonstrated that power system optimization plots may be generated by plotting the combined system efficiency against two system variables. For many heavy duty UAVs, maximum flight-time is also a critical design criterion. Flight-time is dependent primarily on mass and the capacity of the battery pack. However, as battery capacity is increased, the battery mass increases also. Thus there is an optimum battery pack size beyond which further increasing capacity will actually decrease the maximum flight-time. This issue is further compounded by the payload mass of the craft.

Fig. 14 allows the system to be optimized for maximum flight-time by plotting the simulated maximum flight-times against sweeps of payload mass and battery capacity. The simulation assumed a constant cruising thrust of 1.2 times the total craft mass. The craft mass was recalculated on each iteration based on the current battery capacity and payload mass. A time-based

Fig. 14 Maximum flight-time optimization against payload mass and battery capacity.

simulation is then carried out for each x-y value combination. Maximum flight time is calculated as the time at which the battery state of charge (SOC) reaches 20%. Fig 14 suggests that a battery capacity between 2.2 and 3.7 kWh allows the longest maximum flight-time depending on the desired payload capacity of the craft.
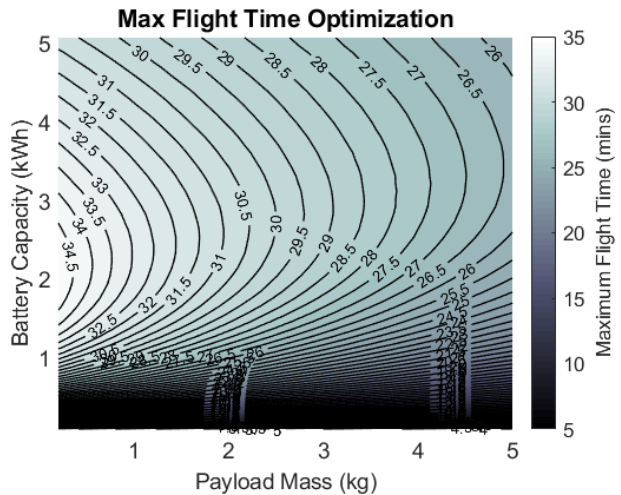
F. Thermal Simulation and Experiments

A variety of results can be generated after figuring out all the coefficients and parameters from Section V. Here is one sample result in Fig. 15. In this plot, the motor stator temperature is modeled and experimentally measured under different motor RPM's and thus different torques. The modeled temperature is reasonably close to measured. There are multiple pieces of information available from this graph. For example, the steady state temperature prediction allows for design optimization to choose the lightest motor while enduring the harshest load requirement (i.e., continuous maximum). For another example, the rise time allows assessing the risk when the motor operates at the absolute maximum load but under only a short period.
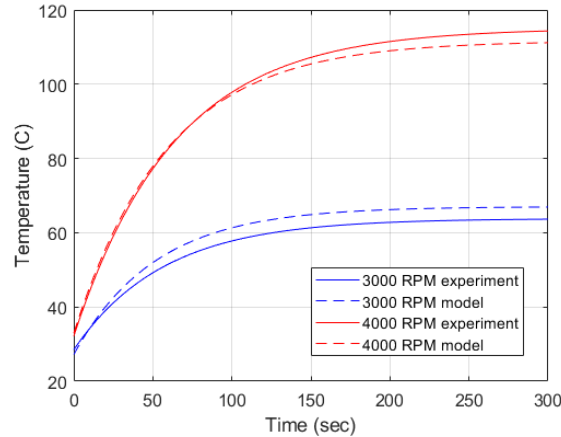
Fig. 15 Modeled and experimental motor stator temperature rises under different motor speeds/loads.

VII. Conclusion

This paper describes various power system architectures for commercial heavy-duty AC motor propelled VTOL UAVs. A comprehensive modeling approach is presented allowing for comparison between architectures or system optimization studies. All modeling and simulation frameworks, in multi-timescales and multi-physics manners, i.e., static, dynamic, electro-mechanical, and thermal, may be applied to any power system, serving as a critical design tool for future VTOL UAVs. Lab-scaled hardware is used to experimentally validate component and system level simulation results. Mission profile based studies allow for system sizing and optimizations. The overall UAV propulsion system is unique in that the motor load is a cubic speed-power related propeller, which at the same time serves as a main air cooling resource to the attached motor.

REFERENCES

[1] Office of the Secretary of Defense, "U.S. Department of Defense Unmanned Aerial Vehicle Road Map 2005 - 2030," 2005.

[2] Google X, "Project Wing," [Online]. Available: https://x.company/projects/wing/.

[3] Amazon, "Amazon Prime Air," [Online]. Available: https://www.amazon.com/Amazon-Prime-Air/b?ie=UTF8&node=8037720011.

[4] DHL, "DHL Parcelcopter," [Online]. Available: https://www.dpdhl.com/en/media-relations/specials/dhl-parcelcopter.html.

[5] Ehang, "Ehang 184," [Online]. Available: http://www.ehang.com/ehang184/.

[6] A. Thurlbeck and Y. Cao, "Analysis and modeling of UAV power system architectures," in *Proc. IEEE Transportation Electrification Conf. (ITEC)*, 2019, pp. 1-8.

[7] Z. Q. Zhu and D. Howe, "Electrical Machines and Drives for Electric, Hybrid, and Fuel Cell Vehicles," *Proceedings of the IEEE,* vol. 95, no. 4, pp. 746-765, 2007.

[8] J. G. Hayes and G. A. Goodarzi, "Introduction to Traction Machines" in *Electric Powertrain: energy systems, power electronics and drives for hybrid, electric and fuel cell vehicles*, Hoboken, NJ: John Wiley & Sons, 2018.

[9] D. Graovac and M. Purschel, "MOSFET Power Losses Calculation Using the Data-Sheet Parameters," Infineon Application Note, 2006.

[10] Y. Cao, R. C. Kroeze and P. T. Krein, "Multi-timescale parametric electrical battery model for use in dynamic electric vehicle simulations," *IEEE Transactions on Transportation Electrification,* vol. 2, no. 4, pp. 432-442, 2016.

[11] N. Mohan, *Advanced Electric Drives: Analysis, Control, and Modeling Using MATLAB / Simulink*. New Jersey: Wiley, 2014.

[12] Y. Cao, M. A. Williams, B. J. Kearbey, A. T. Smith, P. T. Krein, and A. G. Alleyne, "20x-Real Time Modeling and Simulation of More Electric Aircraft Thermally Integrated Electrical Power Systems," in *Proc. IEEE International Conf. Electrical Systems for Aircraft, Railway, Ship Propulsion and Road Vehicles* (*ESARS-ITEC*), 2016, pp. 1-6.

[13] M. E. Dreier and A. Paredes, "A numerical investigation of ground effect on a coaxial rotor system," in *Proc. American Helicopter Society 71st Annual Forum*, 2015, pp. 1-14.